Catalysis Letters (2018) 148:2315–2324
https://doi.org/10.1007/s10562-018-2437-x

Tuning the Core–Shell Structure of $Au_{144}@Fe_2O_3$ for Optimal Catalytic Activity for CO Oxidation

Michelle Lukosi[1,2] · Chengcheng Tian[1,2] · Xinyi Li[1] · Shannon M. Mahurin[3] · Harry M. Meyer III[3] · Guo Shiou Foo[3] · Sheng Dai[1,2,3]

Received: 6 December 2017 / Accepted: 30 May 2018 / Published online: 9 June 2018

Abstract

Core–shell heterostructures have been utilized as a catalyst that is thermally stable and exhibits a synergistic effect between core and shell, resulting in increased catalytic activity. Here we report on the synthetic procedure involving a Au_{144} core with an iron oxide shell which can be varied in thickness. The $Au_{144}@Fe_2O_3$ particles with Au:Fe mass ratios of 1:2, 1:4, and 1:6 were synthesized and then deposited onto silica via colloidal deposition. Using CO oxidation, each $Au_{144}@Fe_2O_3/SiO_2$ catalyst gave varying degrees of full CO conversion depending on the thickness of the iron oxide layer. The 1:4 $Au_{144}@Fe_2O_3/SiO_2$ catalyst produced the best catalytic activity and was further investigated via thermal treatments, where calcination at 300 °C presented the best results, and the 1:4 ratio was still active at 100 °C after thermal treatments.

Graphical Abstract

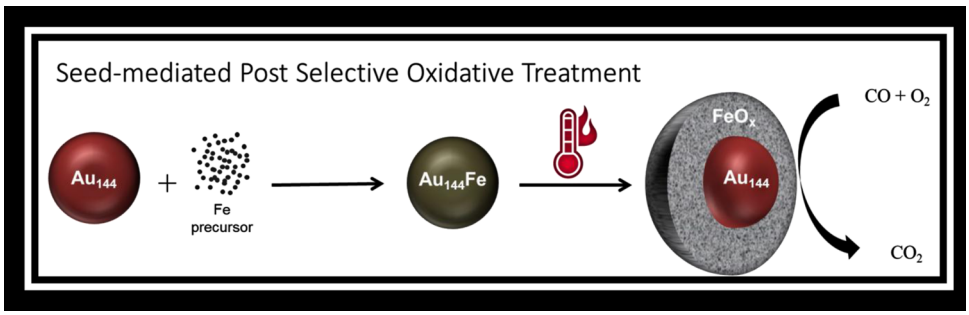

Keywords Catalysis · Core–shell nanoparticles · Au_{144} nanocluster · CO oxidation · 2-Propanol conversion · Thermal treatment

1 Introduction

Carbon monoxide (CO) is an odorless, colorless gas that is lethal in small quantities. It has a permissible exposure limit (PEL) of 50 ppm over an 8-h work period, referred to as the time-weighted average (TWA). The PEL is the maximum amount of chemical substance or physical agent a worker may be exposed to under OSHA regulations. One such solution to diminish CO concentrations is to oxidize it to carbon dioxide (CO_2). The PEL for CO_2 is 5000 ppm TWA, resulting in rare cases of poisoning [1]. This method has practical applications in the industrial sector, such as car emissions, CO_2 lasers for

✉ Sheng Dai
dais@ornl.gov

[1] Department of Chemistry, University of Tennessee-Knoxville, Knoxville, TN 37996-1600, USA

[2] Joint Institute of Advanced Materials, University of Tennessee-Knoxville, Knoxville, TN 37996-1600, USA

[3] Chemical Sciences Division, Oak Ridge National Laboratory, Oak Ridge, TN 37831, USA

welding, medical surgery and spectroscopy, fuel technology, gas sensors, and various chemical processes [2–7].

It was discovered by Haruta et al. [8] that gold nanoparticles are effective for low-temperature CO oxidation [8]. Since this discovery, gold nanoparticles have become a big topic of discussion for catalytic reactions. Valden et al. [9] used a sputtering technique to study gold particles of various sizes with CO oxidation. They found that gold nanoparticles with dimensions of 3.5 by 1.0 nm^2 (approximately 300 atoms per particle) and smaller exhibited a metal-to-nonmetal transition. This transition in gold nanoparticles has been linked to enhanced catalytic activity [10]. Further, gold particles, as well as some other metals like iron and copper [11], exhibit a rise in their redox potential as their size decreases [12] where a higher reduction potential will give rise to higher catalytic activity [13]. Given this trend, small gold nanoclusters could display higher catalytic activity than nanoparticles for some reactions. However, gold nanoparticles < 1 nm in diameter are not very stable [14], which would manifest as a negative effect on their activity [15].

As research into catalytic gold emerged, so did research into small uniform catalysts that could deliver consistent and reproducible results. This opened the door to nanocluster catalysis, where there are a specified number of atoms in each gold particle, whereas nanoparticles typically incorporate a range of sizes. Thiolate-protected gold nanoparticles, first proposed by Brust and Schiffrin [16], has become the building block to obtaining a well-defined $Au_n(SR)_m$ formula using specific Au-to-thiol ratios. Here, the gold cluster with number of atoms, n, corresponds to a certain number of thiolate groups, m, encompassing a sulphur (S) atom and an organic rest group (R), which creates a monolayer surrounding the gold cluster [17, 18].

The Au_{144} nanocluster has been recognized as one of the larger, relatively stable, gold clusters [19–23]. Its structure has been established experimentally, utilizing techniques such as electrospray ionization (ESI), MALDI-MS, STEM, and X-ray spectroscopy [21, 24–26]. Weissker et al. performed time-dependent density-functional theory (TD-DFT) calculations to show individual peaks representing discrete levels of the structures localized electronic states [27]. This means there is a discrete energy band structure that develops for small clusters, hence there is a metal-to-nonmetal transition, similar to that of semiconductors [28]. That being stated, gold nanoparticles by themselves tend to sinter easily, losing their catalytic ability. The smaller the particles, the more this sintering becomes a prominent issue. This is, in large part, why very small gold nanoparticles and clusters are a difficult catalyst to effectively utilize. To stabilize gold nanoparticles, at the very least, they are loaded onto a support. The support is generally a metal oxide [29], but others have reported using other support types, such as carbon-based or titanium(IV) chloride supports [30, 31]. Even with different support structures, small gold nanoparticles (< 10 nm in diameter) sinter above room temperature. In the interest of overcoming this issue, core–shell structures have been investigated [32–47], where the gold nanoparticle/cluster is the core with a protective, often metal oxide, shell. This allows the gold to retain its size and shape, preserving its catalytic ability under thermal and mechanical stress. These core–shell structures have not yet been investigated for small gold clusters, given the cluster's delicate nature. Given the large increase in surface-to-volume ratio for cluster-sized core–shell structures, they are a potential effective catalyst, exhibiting more catalytic sites compared to larger particles of the same volume. For this reason, research into their stabilization is key. This paper seeks to investigate the stability, catalytic properties, and effect of the thickness of an iron oxide shell surrounding Au_{144} clusters.

2 Experimental

2.1 Materials

The chemical reagents used were hydrogen tetrachloroaurate trihydrate ($HAuCl_4{\cdot}3H_2O$), 1-hexanethiol (SHC_6H_{13}, 98%), tetraoctylammonium bromide (TOABr, 98%), sodium borohydride ($NaBH_4$, 99%), iron pentacarbonyl ($Fe(CO)_5$), oleylamine (reagent grade), oleic acid (90%), and Cab-O-Sil (fumed silica). All solvents used were purchased from Fischer Scientific, save deionized water, and were used as received without further purification unless specified otherwise; the list of solvents is as follows: methanol (certified ACS, ≥ 99.8%), toluene (ACS Grade, ≥ 99.5%, LabChem™), acetone (Certified ACS, ≥ 99.5%), ethanol (200 proof (100%), USP, Decon™ Labs), dichloromethane (99.5% min., ACS, EMD Millipore), hexane (certified ACS, ≥ 98.5%), and diphenyl ether (99%, ACROS Organics™).

2.2 Catalyst Preparations

In preparing the Au_{144} clusters, Qian's methods were utilized [19]. In ambient conditions, 0.70 mmol of $HAuCl_4{\cdot}3H_2O$ was added with 0.70 mmol TOABr in methanol in a round bottom flask. The solution changed color from yellow to red, indicating the formation of Oct_4N^+ $AuBr_4^-$. Then, 1.505 mmol of 1-hexanethiol were added to the solution at room temperature and the color of the reaction mixture rapidly turned white. The thiol/Au ratio was adjusted to 4.3:1 based on another groups' modification [27]. After 1 h, a fresh solution of $NaBH_4$ (3.5 mmol) in cold DI water was rapidly added to the solution under vigorous stirring. The color of solution immediately turned black and produced Au clusters, which were then precipitated out of the methanol solution. The reaction continued to stir for 5 h to completely equilibrate the reaction. The black precipitates were then collected by centrifugation

(5 min at 5000 rpm) and decantation. The black precipitates were washed with excess methanol and collected by centrifugation several times to completely remove small-molecule and electrolyte residue, including excess free thiol residues. Then, toluene was used to separate the Au clusters from Au(I)–SR polymers, which are poorly soluble in most solvents. The as-obtained solution only contains $Au_{144}(SR)_{60}$ (major product) and $Au_{25}(SR)_{18}$ (minor product), determined via MALDI and ESI [19, 27, 48]. Acetone was used to separate the $Au_{144}(SR)_{60}$ and $Au_{25}(SR)_{18}$ clusters, where the $Au_{144}(SR)_{60}$ clusters separate out during centrifuge and $Au_{25}(SR)_{18}$ clusters remain dispersed in the acetone solution. The $Au_{144}(SR)_{60}$ clusters can be dispersed into hexane, toluene, or dichloromethane depending on characterization. To determine yield, an empty vial was weighed, a Au_{144} solution was added, and then the solution was dried to determine the weight of clusters. Afterwards, the clusters were dispersed into a determined amount of solution, creating a known concentration. In this way, 20 mg of the clusters can be extracted into another vial for use in the second step to this experiment. To ensure an exact amount was used, this solution was re-weighed out in the same fashion.

In coating the cluster with an iron oxide shell, methods from Yin et al. were applied [33]. In a 4-neck 100 mL round-bottom flask, 50 mL of diphenyl ether, 0.15 mL of an oleylamine, and 0.15 mL oleic acid were added and stirred for 5 min. Then, 20 mg of Au_{144} clusters dispersed in 2 mL of toluene was added to the mixture. The solution was set to stir under nitrogen flow and heated at 80 °C for 30 min. The reaction was put under a nitrogen blanket before adding the iron pentacarbonyl in varying amounts. The flask was slowly heated to 200 °C and left to stir for 30 min. The reaction was then left to cool to approximately 100 °C and then the N_2 environment was removed and air was flowed through the flask for a minimum of 10 min to allow the iron to oxidize. Subsequently, the reaction flask was allowed to cool to room temperature. The solution was washed with ethanol and centrifuged and the core–shell precipitate was then dispersed in hexane.

To analyze and test the core–shell structures, they were deposited onto fumed silica (SiO_2) using ~ 1.5% gold loading. Fumed silica support was utilized because of its inert properties, given its weak metal support interaction (WMSI) and ability to adsorb cations, as opposed to other metal oxide supports that have strong metal support interactions (SMSI's). The silica (Cab-O-Sil) was added to the colloidal mixture of $Au_{144}@Fe_2O_3$ core-shell particles in hexane, sonicated, and stirred for 2 h before slowly evaporating off the solvent, using rotary evaporation. After removing the solvent, the powder was dried and calcined at 300 °C for 2 h.

2.3 Characterizations

The Au_{144} clusters were characterized by utilizing a Bruker matrix assisted laser desorption ionization time-of-flight mass spectrometer (MALDI-TOF-MS) and X-ray diffraction (XRD). The mass spectrum was collected in a linear positive ion mode. A dichloromethane solution of the $Au_{144}(SR)_{60}$ particles (5 mg/mL) were mixed with the matrix, a chloroform solution of trans-2-[3-(4-tert-butylphenyl)-2-methyl-2-propenylidene]malononitrile (DCTB), applied to the sample plate, and air dried. XRD data of the clusters was gathered by studying thin films of the particles. At room temperature, the clusters were analyzed using a PANalytical Empyrean diffractometer over the range from 10° to 80° 2θ using Cu Kα at wavelength 1.540958 Å radiation at 45 kV and 40 mA.

The $Au_{144}@Fe_2O_3$ core–shell structures were characterized by XRD, for which the data of the core–shell structures were collected by studying powder samples of the silica loaded systems and analyzed using the same instrumentation and parameters as those used for the Au_{144} thin films. The nitrogen physisorption isotherms were measured at 77 K using a Gemini 2375 Brunauer–Emmett–Teller (BET) surface area analyzer. Elemental analysis was done by inductively coupled plasma optical emission spectroscopy (ICP-OES), using an Optima 2100 DV optical emission spectrometer (PerkinElmer Corporation). Visual measurements were operated on Hitachi HD-2000 scanning transmission electron microscopy (STEM) and with high-angle annular dark-field (HAADF) techniques with the aid of ImageJ, the samples were dispersed in ethanol or hexanes assisted by ultrasonic technique. Oxidation states of the metals were determined via X-ray photoelectron spectroscopy (XPS). All XPS data was attained using a Phi 3056 spectrometer equipped with an aluminum anode source operated at 15 kV, an applied power of 350 W, and a pass energy of 93.5 eV.

The catalytic activity of the core–shell structures were tested by analyzing its ability to oxidize CO to CO_2. 20 mg of the $Au_{144}@Fe_2O_3$ catalyst was packed into a quartz tube (inner diameter = 4 mm) sealed on either side by quartz wool, a gas stream of 1% CO (balance air) flowed through the catalyst at a rate of 10 mL/min, and the exiting stream was analyzed by a gas chromatograph equipped with a dual molecular sieve/porous polymer column, a thermal conductivity detector, and a gas hourly space velocity (GHSV) of 30,000 mL $(h\ g_{cat})^{-1}$. The reaction temperature was controlled using a voltage transformer attached to a furnace. In addition, Fourier transform infrared (FTIR) spectroscopy was able to determine CO adsorption on the structure. With the core–shell structures loaded onto fumed silica and calcined at a certain temperature, FTIR spectroscopy was obtained at a temperature of 5 °C. A spectrum was taken after 10 min of 2% CO flowing over the loaded structure, with any spectral contribution from gaseous CO subtracted. Then, spectra were taken after purging the

sample with 2% He for 3 and 10 min. Similar research done by Yin et al. was completed using gold nanoparticles 2–5 nm in diameter with varied iron oxide shell thicknesses tested for catalytic activity using CO oxidation. While many of these authors share authorship with Yin et al. [33], access to the previous instrument was not possible, so a one-to-one comparison was not possible. Regardless, the different diameters of both the Au core and Fe_2O_3 shell as well as the loading of each to the substrate (silica) will undoubtedly yield different results. Also, of note is that with bigger particles Yin et al. were able to get higher Au loading (~3.5%), while we were unable to get above 2% Au loading with smaller particles.

3 Results and Discussion

3.1 $Au_{144}(SC_6H_{13})_{60}$ Nanocluster

The MALDI-TOF mass spectrum of the Au_{144} clusters with 1-hexanethiol capping is expected to show a broad peak at approximately 32,500 Da [19, 27], as shown in Fig. 1, even though the total structure itself is calculated to be 35,397 Da. The peak position shift of roughly 2900 Da is due to partial loss and fragmentation of the thiol–gold (–RS–Au–SR–) staple motifs from the laser intensity under the MALDI conditions [19], where each staple motif contributes ~ 430 Da to the total mass of the structure. Each $Au_{144}(SR)_{60}$ cluster has been previously calculated by other groups to have 30 staple motifs, which include 30 of the 144 Au atoms in the capping structure [27]. For further characterization of the clusters, thin film XRD measurements were taken (Fig. 2). The small broad peak, with FWHM being 5.16° 2θ and centered at

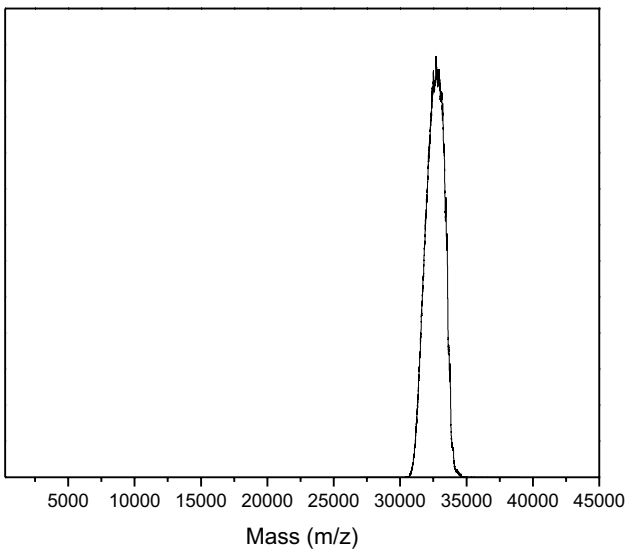

Fig. 1 MALDI-TOF-MS of $Au_{144}(SC_6H_{13})_{60}$ with peak at 32,500 m/z (Da)

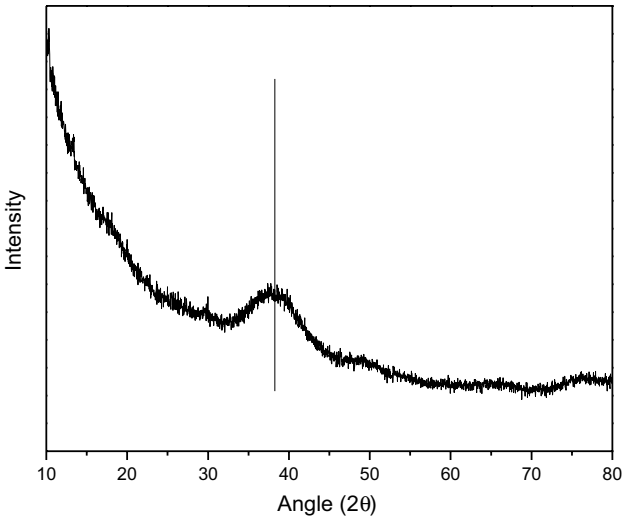

Fig. 2 XRD of $Au_{144}(SC_6H_{13})_{60}$ thin film with broad peak at 38.58° 2θ indicative of small Au domain

38.58° 2θ, indicates the Au cluster has a domain of approximately 1.7 nm in diameter, via the Scherrer equation [49]. This correlates well with DFT estimations of ~ 1.6 nm, calculated by Weissker et al. [27].

3.2 $Au_{144}@Fe_2O_3$: Effect of Shell Thickness

The thickness of the iron oxide shell was controlled by varying the amount of iron precursor added during the reaction. The different $Au_{144}@Fe_2O_3$ core–shell structures are referred

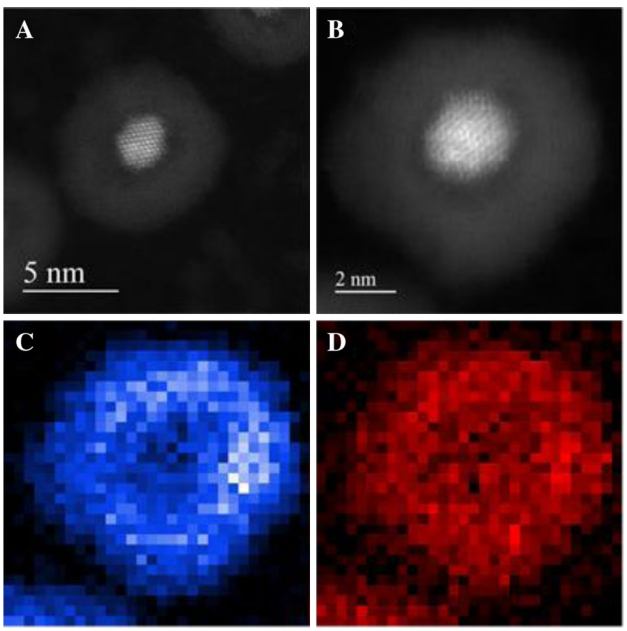

Fig. 3 **a, b** HAADF of 1:4 $Au_{144}@Fe_2O_3$ structure as synthesized, as well as the **c** Fe (blue) and **d** O (red) areal density of structure (**b**)

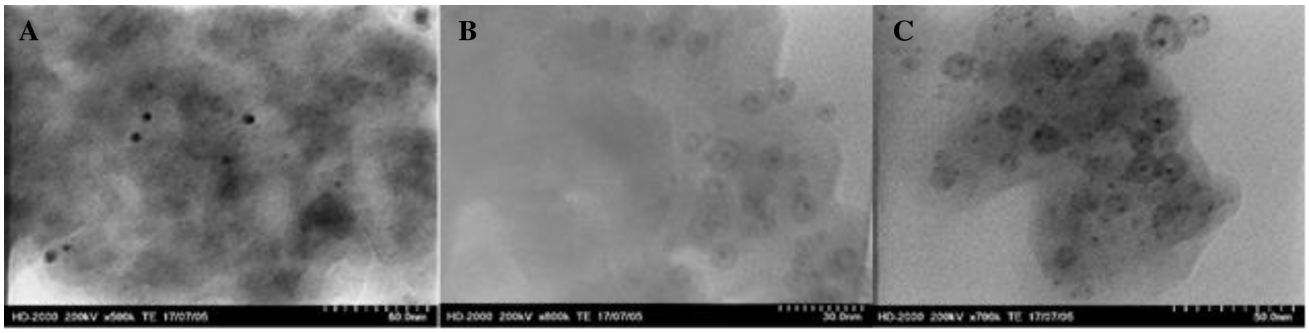

Fig. 4 STEM of $Au_{144}@Fe_2O_3/SiO_2$ with varying Fe_2O_3 content for the **a** 1:2, **b** 1:4, and **c** 1:6 structures

Table 1 BET surface area and ICP-OES weight percent of core–shell structure loaded onto silica

Au–Fe ratios by mass	SA_{BET} (m^2/g)	Au_{ICP} (wt%)	Fe_{ICP} (wt%)
$mSiO_2$	356	–	–
1:2	136	1.2	5.8
1:4	183	1.7	7.5
1:6	171	1.5	9.2

to by their Au:Fe ratios by mass. The structures studied in this paper were 1:2, 1:4, and 1:6. HAADF–STEM images of the 1:4 structures, prior to being loaded and before calcination, show a small Au_{144} particle surrounded by an iron oxide shell (Fig. 3). There is a small gap at the core–shell interface, which is believed to be indicative of the thiol capping still attached to the gold cluster.

Once calcined to 300 °C, the thiol capping and other organic residuals, which includes any solvent surfactants that may still be in solution, are removed with the purpose of activating the gold catalysts. The structures that were fully covered reveal a yolk–shell like structure, as has been seen in other literature [41, 50–54], rather than strictly a core–shell design (Fig. 4b, c). This is due to the removal of thiol capping agent on the gold cluster, which winds up leaving a gap, or void, between the core and shell.

In our studies, a threshold limit was discovered for an optimal metal oxide shell of this particular morphology. When too little of the iron precursor ($Fe(CO)_5$) was added, the metal oxide was unable to cover the cluster completely, which led to sintering under calcination, as was the case with the Au:Fe 1:2 structure, and revealed a dumbbell-like structure (Fig. 4a), as has been seen in other literature [37, 55, 56]. The threshold amount may be different with a different thiol capping. For the 1:4 structure, the Fe_2O_3 shell was approximately 1.5 nm thick, while the 1:6 structure was approximately 2.5 nm thick, estimated via STEM. According to BET results, the surface area is larger for the 1:4 versus the 1:6 structure (Table 1).

Bulk gold has a face-centered-cubic (fcc) crystal structure, and when analyzed with XRD, there will be a predominant peak at 38.2° 2θ and less predominant peaks at 44.4°, 64.5°, and 77.5° 2θ representing the (111), (200), (220),

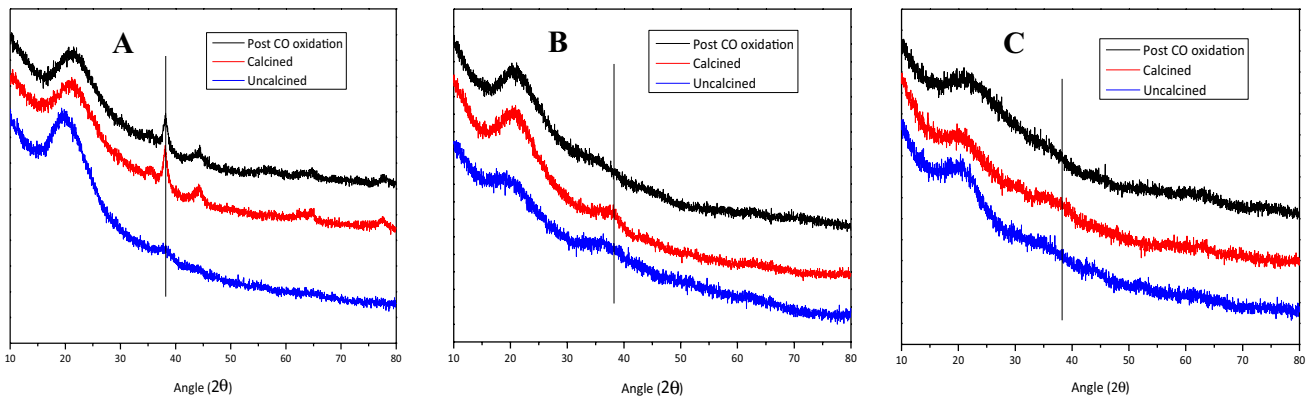

Fig. 5 XRD of $Au_{144}@Fe_2O_3/SiO_2$ with varying Fe_2O_3 content for **a** 1:2, **b** 1:4, and **c** 1:6 structures, with a line at 38.2° 2θ where bulk gold peaks are prominent

and (311) surface planes, respectively (Joint Committee on Powder Diffraction Standards-International Center for Diffraction Data (JCPDS-ICDD) file #04-0784). However, very small particles (< 2 nm) can be quite difficult to detect and XRD is no exception [57]. Some other factors to consider in these measurements is that the iron oxide shell is amorphous in nature, as well as the weight fraction of gold being very small. With the Au_{144} clusters, there is barely a hump at the prominent angle at 38° 2θ, with the exception of the 1:2 structure (Fig. 5). After calcination, it is clear that the 1:2 structures sintered as that peak becomes sharper and more defined, representative of larger gold particles. This

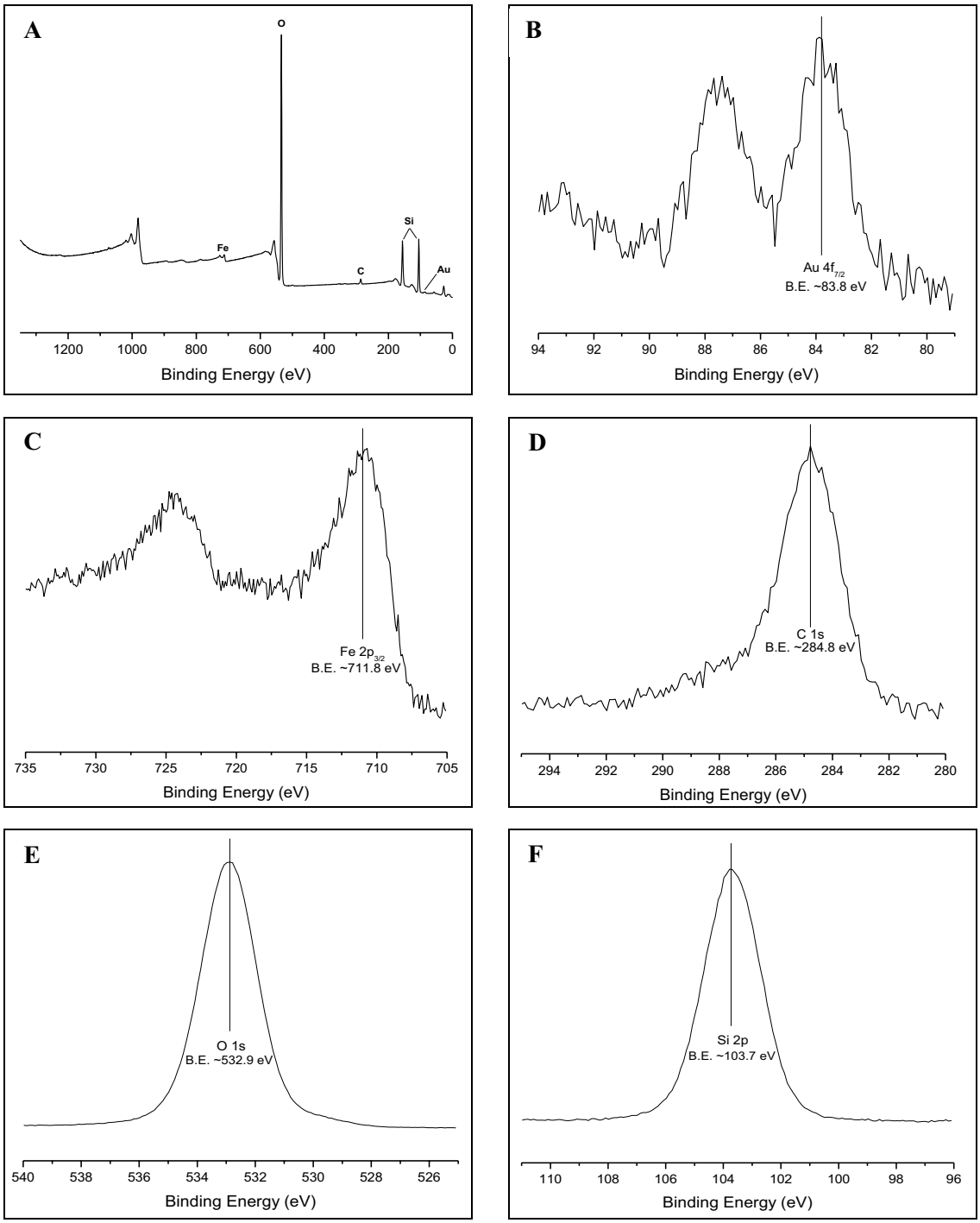

Fig. 6 XPS of surface composition of $Au_{144}@Fe_2O_3$ 1:4 structure showing **a** the survey spectrum and the high-resolution spectra of **b** gold, **c** iron, **d** oxygen, **e** silicon, and **f** carbon

Table 2 XPS—surface composition (at.%): $Au_{144}@Fe_2O_3$

Au	Fe	Si	O	C
0.06	1.12	31.49	63.17	3.85

corroborates with the STEM images, that the iron oxide shell was unable to cover the particle completely, and, without the protective shell, the Au_{144} clusters coalesced. For the 1:4 and 1:6 structures, no sintering was visible from the XRD spectra, which is indicative of full coverage of the amorphous iron oxide shell, as the STEM images indicate.

XPS of the 1:4 structure, which was loaded onto fumed silica and calcined at 300 °C, provided a survey spectrum, or wide-scan showing all elements present (Fig. 6a), with subsequent high resolution (core level) spectra of each element identified (Fig. 6b–f), as well as the overall percentage surface composition that each element contributes (Table 2). The binding energy position of the main Au 4f peak is at 83.8 eV, indicative of a metallic Au species [58]. This is merely a slight shift of − 0.2 eV in the binding energy for the Au $4f_{7/2}$ peak from 84.0 eV, which is typically seen for bulk gold [59–62]. The binding energy position of the Fe $2p_{3/2}$ peak is at 711.8 eV, indicative of a primary 3^+ valence [63], which means the iron oxide shell is in the Fe_2O_3 structure, with a + 0.4 eV shift from that typically measured at 711.4 eV [64–68]. The O 1s orbital is primarily associated with the Si 2p orbital from the SiO_2 support. The C 1s signal was relatively low and is predominantly adsorbed carbonaceous material during analysis.

3.3 Synergistic Effects of Core–Shell System

Using control experiments of Au_{144} nanoclusters and Fe_2O_3 nanoparticles loaded onto silica, (Au_{144}/SiO_2 and Fe_2O_3/SiO_2, respectively) we were able to compare with the $Au_{144}@Fe_2O_3/SiO_2$ core–shell particles. Using CO oxidation tests, the synergistic effects of the core–shell structures are apparent by comparison of each structures catalytic abilities (Fig. 7). For the core–shell structures, full oxidation of CO for the 1:2, 1:4 and 1:6 structures occurred at 211, 75, and 111 °C, respectively. Au_{144} nanoclusters by themselves showed some oxidation at room temperature, but did not exhibit full oxidation of CO until ~ 500 °C. Whereas, Fe_2O_3 nanoparticles by themselves never reached full CO oxidation, up to 500 °C. The Au_{144} nanoclusters were determined to have sintered into larger particles, and more evidence that sintering occurred was that the catalyzed Au_{144} particles visibly appeared a red/purple color after testing was completed.

To further investigate the behavior of CO adsorption onto the $Au_{144}@Fe_2O_3$ particle and obtain more information about the Fe_2O_3 surface, FTIR spectroscopy of the 1:4 core–shell structure, loaded onto fumed silica and

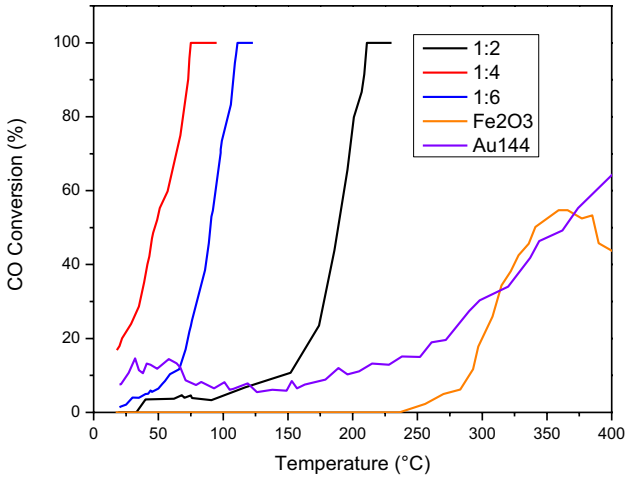

Fig. 7 CO conversion on $Au_{144}@Fe_2O_3/SiO_2$ catalysts with varying Fe_2O_3 shell thickness, as well as Fe_2O_3/SiO_2 and Au_{144}/SiO_2

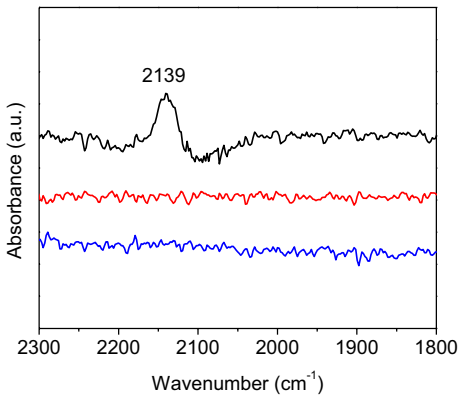

Fig. 8 FTIR of CO adsorption onto 1:4 structure $Au_{144}@Fe_2O_3/SiO_2$ at 5 °C (gaseous CO contribution subtracted)

calcined at 300 °C, was obtained at 5 °C (Fig. 8). The top spectrum was taken after 10 min of 2% CO flow. The middle and bottom spectra were taken after purging the sample with 2% He for 3 and 10 min, respectively. There was only one distinct peak at 2139 cm^{-1}, from the top spectrum, which can be attributed to CO being adsorbed onto a positively charged Au species ($Au^{\delta+}$, $0 < \delta < 1$) [69, 70]. The middle and bottom spectra showed no distinct peaks, which signifies that the CO was readily desorbed from the catalyst surface. The positively charged Au species is attributed to the iron oxide layer that is surrounding the Au core. Only during the process of CO oxidation, while CO is adsorbed, is this positive Au species observed.

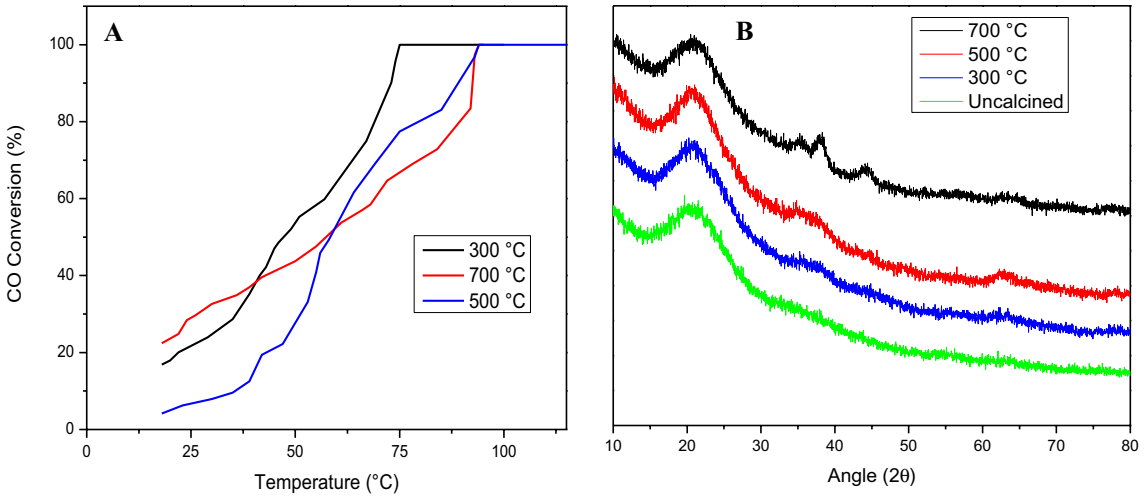

Fig. 9 The 1:4 $Au_{144}@Fe_2O_3/SiO_2$ structure calcined at temperatures 300, 500 and 700 °C showing **a** CO conversion and **b** XRD spectra

3.4 Thermal Treatments of 1:4 $Au_{144}@Fe_2O_3$ Structure

The 1:4 structure, with the best CO oxidation results, was put through varying thermal treatments to test the structure's optimal activity. The structure was tested at pretreatments of 300, 500, and 700 °C. Results for the 300 °C pretreatments showed the best activity with full conversion at 75 °C (Fig. 9a). It should be noted, however, that the 1:4 structure showed full conversion at 95 °C for both pretreatments at 500 and 700 °C. Although the higher temperature pretreatments do not display the best catalytic activity, it is still active below 100 °C, which is more efficient than the 1:6 structure pretreated at 300 °C. This indicates thermal stability at these higher calcination temperatures. However, the XRD for these 1:4 samples (Fig. 9b) show some sintering as the pretreatment temperature is increased, where the peaks become more defined, particularly at 38.2° 2θ, where bulk gold is typically represented.

4 Conclusions

$Au_{144}@Fe_2O_3$ core–shell structures were synthesized with varying shell thickness by varying the metal oxide precursor used. These structures were loaded onto a fumed silica support via colloidal deposition, calcined at 300 °C, and the structure's catalytic activities were compared based on the efficiency of CO oxidation. Between the $Au_{144}@Fe_2O_3/SiO_2$ structures 1:2, 1:4, and 1:6 structures, the 1:4 structure exhibited 100% oxidation of CO at the lowest temperature, 75 °C, and the 1:6 structure, with a thicker iron oxide shell, reached full oxidation of CO at a slightly higher temperature, 111 °C. The 1:2 structure did not result in full core coverage, which is why it exhibited poor CO oxidation properties compared to the 1:4 and 1:6 structures and represents a minimum threshold of Fe_2O_3 shell thickness. Based on these results, the 1:4 structure was studied under thermal treatments of 300, 500, and 700 °C, followed by CO oxidation. The results showed that the best results for the 1:4 structure was at 300 °C pretreatment, however, higher temperature pretreatments still showed promising results.

Acknowledgements This work was supported by the U.S. Department of Energy, Office of Science, Chemical Sciences, Geosciences and Biosciences Division. Synthetic procedures were conducted at the Joint Institute of Advanced Materials at the University of Tennessee. XPS and FTIR data were acquired by Harry M. Meyer III and Guo Shiou Foo, respectively, at Oak Ridge National Laboratory.

Compliance with Ethical Standards

Conflict of interest The authors declare no competing financial interest.

References

1. Carbon dioxide Atlanta, GA [cited CDC Centers for Disease Control and Prevention]. http://www.cdc.gov/niosh/npg/npgd0103.html
2. Qi J, Chen J, Li G, Li S, Gao Y, Tang Z (2012) Facile synthesis of core–shell $Au@CeO_2$ nanocomposites with remarkably enhanced catalytic activity for CO oxidation. Energy Environ Sci 5(10):8937–8941
3. Chen L, Chang B-K, Lu Y, Yang W, Tatarchuk BJ (2002) Selective catalytic oxidation of CO for fuel cell application. Fuel Chem Div Prepr 47(2):609–610
4. Kandoi S, Gokhale A, Grabow L, Dumesic J, Mavrikakis M (2004) Why Au and Cu are more selective than Pt for preferential oxidation of CO at low temperature. Catal Lett 93(1–2):93–100

5. Tsuchida E, Sato H (1990) Recovery of transient gain in an open-cycle FAF CO_2 laser amplifier using gold catalyst. Jpn J Appl Phys 29(6A):L964
6. Levine R, Vitruk P, MlnstP C (2015) Laser-assisted operculectomy. Compend Contin Educ Dent 36:561–567
7. Ando M, Kobayashi T, Iijima S, Haruta M (1997) Optical recognition of CO and H_2 by use of gas-sensitive Au–Co_3O_4 composite films. J Mater Chem 7(9):1779–1783
8. Haruta M, Kobayashi T, Sano H, Yamada N (1987) Novel gold catalysts for the oxidation of carbon monoxide at a temperature far below 0. DEG. C. Chem Lett 16(2):405–408
9. Valden M, Lai X, Goodman DW (1998) Onset of catalytic activity of gold clusters on titania with the appearance of nonmetallic properties. Science 281(5383):1647–1650
10. Bond GC (2011) The effect of the metal to non-metal transition on the activity of gold catalysts. Faraday Discuss 152:277–291
11. Ponec V, Bond GC (1995) Catalysis by metals and alloys. Elsevier, Amsterdam
12. Bond GC, Louis C, Thompson DT (2006) Catalysis by gold. World Scientific, Singapore
13. Kovala-Demertzi D, Hadjikakou SK, Demertzis MA, Deligiannakis Y (1998) Metal ion–drug interactions. Preparation and properties of manganese (II), cobalt (II) and nickel (II) complexes of diclofenac with potentially interesting anti-inflammatory activity: behavior in the oxidation of 3, 5-di-tert-butyl-o-catechol. J Inorg Biochem 69(4):223–229
14. Overbury S, Schwartz V, Mullins DR, Yan W, Dai S (2006) Evaluation of the Au size effect: CO oxidation catalyzed by Au/TiO_2. J Catal 241(1):56–65
15. Che M, Bennett CO (1989) The influence of particle size on the catalytic properties of supported metals. Adv Catal 36:55–172
16. Brust M, Walker M, Bethell D, Schiffrin DJ, Whyman R (1994) Synthesis of thiol-derivatised gold nanoparticles in a two-phase liquid–liquid system. J Chem Soc Chem Commun. https://doi.org/10.1039/C39940000801
17. Chen T, Luo Z, Yao Q, Yeo AXH, Xie J (2016) Synthesis of thiolate-protected Au nanoparticles revisited: U-shape trend between the size of nanoparticles and thiol-to-Au ratio. Chem Commun 52(61):9522–9525
18. Azubel M, Kornberg RD (2016) Synthesis of water-soluble, thiolate-protected gold nanoparticles uniform in size. Nano Lett 16(5):3348–3351
19. Qian H, Jin R (2011) Ambient synthesis of $Au_{144}(SR)_{60}$ nanoclusters in methanol. Chem Mater 23(8):2209–2217
20. Chaki NK, Negishi Y, Tsunoyama H, Shichibu Y, Tsukuda T (2008) Ubiquitous 8 and 29 kDa gold: alkanethiolate cluster compounds: mass-spectrometric determination of molecular formulas and structural implications. J Am Chem Soc 130(27):8608–8610
21. Jin R, Qian H, Wu Z, Zhu Y, Zhu M, Mohanty A et al (2010) Size focusing: a methodology for synthesizing atomically precise gold nanoclusters. J Phys Chem Lett 1(19):2903–2910
22. Liu J, Jian N, Ornelas I, Pattison AJ, Lahtinen T, Salorinne K et al (2017) Exploring the atomic structure of 1.8 nm monolayer-protected gold clusters with aberration-corrected STEM. Ultramicroscopy 176:146–150
23. Guryanov I, Polo F, Ubyvovk EV, Korzhikova-Vlakh E, Tennikova T, Rad AT et al (2017) Polylysine-grafted Au_{144} nanoclusters: birth and growth of a healthy surface-plasmon-resonance-like band. Chem Sci 8(4):3228–3238
24. Qian H, Zhu M, Wu Z, Jin R (2012) Quantum sized gold nanoclusters with atomic precision. Acc Chem Res 45(9):1470–1479
25. Bahena D, Bhattarai N, Santiago U, Tlahuice A, Ponce A, Bach SB et al (2013) STEM electron diffraction and high-resolution images used in the determination of the crystal structure of the $Au_{144}(SR)_{60}$ cluster. J Phys Chem Lett 4(6):975–981
26. MacDonald MA, Zhang P, Qian H, Jin R (2010) Site-specific and size-dependent bonding of compositionally precise gold–thiolate nanoparticles from X-ray spectroscopy. J Phys Chem Lett 1(12):1821–1825
27. Weissker H-C, Escobar HB, Thanthirige V, Kwak K, Lee D, Ramakrishna G et al (2014) Information on quantum states pervades the visible spectrum of the ubiquitous $Au_{144}(SR)_{60}$ gold nanocluster. Nat Commun 5:3785
28. Haruta M (2011) Spiers memorial lecture role of perimeter interfaces in catalysis by gold nanoparticles. Faraday Discuss 152:11–32
29. Haruta M (2002) Catalysis of gold nanoparticles deposited on metal oxides. Cattech 6(3):102–115
30. Hill AF (2002) Organotransition metal chemistry. Royal Society of Chemistry, Cambridge
31. Huang H, Wang X (2014) Recent progress on carbon-based support materials for electrocatalysts of direct methanol fuel cells. J Mater Chem A 2(18):6266–6291
32. Lin F-h, Doong R-a (2011) Bifunctional Au–Fe_3O_4 heterostructures for magnetically recyclable catalysis of nitrophenol reduction. J Phys Chem C 115(14):6591–6598
33. Yin H, Ma Z, Chi M, Dai S (2011) Heterostructured catalysts prepared by dispersing $Au@Fe_2O_3$ core–shell structures on supports and their performance in CO oxidation. Catal Today 160(1):87–95
34. Zhuang Z, Sheng W, Yan Y (2014) Synthesis of monodisperse $Au@Co_3O_4$ core-shell nanocrystals and their enhanced catalytic activity for oxygen evolution reaction. Adv Mater 26(23):3950–3955
35. Tripathy SK, Mishra A, Jha SK, Wahab R, Al-Khedhairy AA (2013) Synthesis of thermally stable monodispersed $Au@SnO_2$ core–shell structure nanoparticles by a sonochemical technique for detection and degradation of acetaldehyde. Anal Methods 5(6):1456–1462
36. Janardhanan VM, Deutschmann O (2006) CFD analysis of a solid oxide fuel cell with internal reforming: coupled interactions of transport, heterogeneous catalysis and electrochemical processes. J Power Sources 162(2):1192–1202
37. Zhu H, Sigdel A, Zhang S, Su D, Xi Z, Li Q et al (2014) Core/shell Au/MnO nanoparticles prepared through controlled oxidation of AuMn as an electrocatalyst for sensitive H_2O_2 detection. Angew Chem 126(46):12716–12720
38. Zhu Z, Chang J-L, Wu R-J (2015) Fast ozone detection by using a core–shell $Au@TiO_2$ sensor at room temperature. Sens Actuators B 214:56–62
39. Mitsudome T, Yamamoto M, Maeno Z, Mizugaki T, Jitsukawa K, Kaneda K (2015) One-step synthesis of core-gold/shell-ceria nano-material and its catalysis for highly selective semihydrogenation of alkynes. J Am Chem Soc 137:13452–13455
40. Wei Y, Zhao Z, Yu X, Jin B, Liu J, Xu C et al (2013) One-pot synthesis of core–shell $Au@CeO_{2-\delta}$ nanoparticles supported on three-dimensionally ordered macroporous ZrO_2 with enhanced catalytic activity and stability for soot combustion. Catal Sci Technol 3(11):2958–2970
41. Jiang G, Huang Y, Zhang S, Zhu H, Wu Z, Sun S (2016) Controlled synthesis of Au–Fe heterodimer nanoparticles and their conversion into Au–Fe_3O_4 heterostructured nanoparticles. Nanoscale 8(41):17947–17952
42. Jiang W, Zhou Y, Zhang Y, Xuan S, Gong X (2012) Superparamagnetic $Ag@Fe_3O_4$ core–shell nanospheres: fabrication, characterization and application as reusable nanocatalysts. Dalton Trans 41(15):4594–4601
43. Teng X, Black D, Watkins NJ, Gao Y, Yang H (2003) Platinum-maghemite core–shell nanoparticles using a sequential synthesis. Nano Lett 3(2):261–264

44. Lin K-C, del Valle C, Huang Y-F (eds) (2014) Synthesis of gold@iron oxide core-shell nanostructures via an electrochemical procedure. In: Meeting Abstracts. The Electrochemical Society
45. Shevchenko EV, Bodnarchuk MI, Kovalenko MV, Talapin DV, Smith RK, Aloni S et al (2008) Gold/iron oxide core/hollow-shell nanoparticles. Adv Mater 20(22):4323–4329
46. Tang Z, Zhang W, Li Y, Huang Z, Guo H, Wu F et al (2016) Gold catalysts supported on nanosized iron oxide for low-temperature oxidation of carbon monoxide and formaldehyde. Appl Surf Sci 364:75–80
47. Kang Y, Ye X, Chen J, Qi L, Diaz RE, Doan-Nguyen V et al (2013) Engineering catalytic contacts and thermal stability: gold/iron oxide binary nanocrystal superlattices for CO oxidation. J Am Chem Soc 135(4):1499–1505
48. Kothalawala N, Kumara C, Ferrando R, Dass A (2013) $Au_{144-x}Pd_x(SR)_{60}$ nanomolecules. Chem Commun 49(92):10850–10852
49. dell'Erba IE, Hoppe CE, Williams RJJ (2012) Films of covalently bonded gold nanoparticles synthesized by a sol–gel process. J Nanopart Res 14(9):1–8
50. Arnal PM, Comotti M, Schüth F (2006) High-temperature-stable catalysts by hollow sphere encapsulation. Angew Chem 118(48):8404–8407
51. Galeano C, Güttel R, Paul M, Arnal P, Lu AH, Schüth F (2011) Yolk-shell gold nanoparticles as model materials for support-effect studies in heterogeneous catalysis: Au, @C and Au, @ZrO_2 for CO oxidation as an example. Chem Eur J 17(30):8434–8439
52. Fan C-M, Zhang L-F, Wang S-S, Wang D-H, Lu L-Q, Xu A-W (2012) Novel CeO_2 yolk–shell structures loaded with tiny Au nanoparticles for superior catalytic reduction of p-nitrophenol. Nanoscale 4(21):6835–6840
53. Evangelista V, Acosta B, Miridonov S, Smolentseva E, Fuentes S, Simakov A (2015) Highly active Au-CeO_2@ZrO_2 yolk–shell nanoreactors for the reduction of 4-nitrophenol to 4-aminophenol. Appl Catal B 166:518–528
54. Wang S, Zhang M, Zhang W (2011) Yolk–Shell catalyst of single Au nanoparticle encapsulated within hollow mesoporous silica microspheres. ACS Catal 1(3):207–211
55. Huang C-C, Yang Z, Chang H-T (2004) Synthesis of dumbbell-shaped Au–Ag core–shell nanorods by seed-mediated growth under alkaline conditions. Langmuir 20(15):6089–6092
56. Han CW, Choksi T, Milligan C, Majumdar P, Manto M, Cui Y et al (2017) A discovery of strong metal–support bonding in nanoengineered Au–Fe_3O_4 dumbbell-like nanoparticles by in situ transmission electron microscopy. Nano Lett 17(8):4576–4582
57. Wojcieszak R, Genet M, Eloy P, Ruiz P, Gaigneaux E (2010) Determination of the size of supported Pd nanoparticles by X-ray photoelectron spectroscopy. Comparison with X-ray diffraction, transmission electron microscopy, and H_2 chemisorption methods. J Phys Chem C 114(39):16677–16684
58. Visco A (1999) X-ray photoelectron spectroscopy of Au/Fe_2O_3 catalysts. Phys Chem Chem Phys 1(11):2869–2873
59. Figueiredo N, Carvalho N, Cavaleiro A (2011) An XPS study of Au alloyed Al–O sputtered coatings. Appl Surf Sci 257(13):5793–5798
60. Kruse N, Chenakin S (2011) XPS characterization of Au/TiO_2 catalysts: binding energy assessment and irradiation effects. Appl Catal A 391(1–2):367–376
61. Peters S, Peredkov S, Neeb M, Eberhardt W, Al-Hada M (2013) Size-dependent XPS spectra of small supported Au-clusters. Surf Sci 608:129–134
62. Anderson DP, Alvino JF, Gentleman A, Al Qahtani H, Thomsen L, Polson MI et al (2013) Chemically-synthesised, atomically-precise gold clusters deposited and activated on titania. Phys Chem Chem Phys 15(11):3917–3929
63. Suzuki S, Yanagihara K, Hirokawa K (2000) XPS study of oxides formed on the surface of high-purity iron exposed to air. Surf Interface Anal 30(1):372–376
64. Allen GC, Curtis MT, Hooper AJ, Tucker PM (1974) X-ray photoelectron spectroscopy of iron–oxygen systems. J Chem Soc Dalton Trans. https://doi.org/10.1039/DT9740001525
65. Wang GY, Lian HL, Zhang WX, Jiang DZ, Wu TH (2002) Stability and deactivation of Au/Fe_2O_3 catalysts for CO oxidation at ambient temperature and moisture. Kinet Catal 43(3):433–442
66. Kurtz RL, Henrich VE (1983) Geometric structure of the α-Fe_2O_3 (001) surface: a LEED and XPS study. Surf Sci 129(2–3):345–354
67. Grosvenor A, Kobe B, Biesinger M, McIntyre N (2004) Investigation of multiplet splitting of Fe 2p XPS spectra and bonding in iron compounds. Surf Interface Anal 36(12):1564–1574
68. McIntyre N, Zetaruk D (1977) X-ray photoelectron spectroscopic studies of iron oxides. Anal Chem 49(11):1521–1529
69. Wu Z, Jiang D-e, Mann AK, Mullins DR, Qiao Z-A, Allard LF et al (2014) Thiolate ligands as a double-edged sword for CO oxidation on CeO_2 supported $Au_{25}(SCH_2CH_2Ph)_{18}$ nanoclusters. J Am Chem Soc 136(16):6111–6122
70. Wu Z, Zhou S, Zhu H, Dai S, Overbury SH (2009) DRIFTS-QMS study of room temperature CO oxidation on Au/SiO_2 catalyst: nature and role of different Au species. J Phys Chem C 113(9):3726–3734